Wafer-scale fabrication of two-dimensional $PtS_2/PtSe_2$ heterojunctions for efficient and broadband photodetection

Jian Yuan[†,//] *Tian sun*,[†,//] *Zhixin Hu*[‡,//] *Wenzhi Yu*,[†] *Weiliang Ma*,[†] *Kai Zhang, Qiaoliang Bao*,[§] *Shu Ping Lau*,[#] *Shenghuang Lin*[#] *and Shaojuan Li*[†,*]

[†]Institute of Functional Nano and Soft Materials (FUNSOM), Jiangsu Key Laboratory for Carbon-Based Functional Materials and Devices, Collaborative Innovation Center of Suzhou Nano Science and Technology, and Joint International Research Laboratory of Carbon-Based Functional Materials and Devices, Soochow University, Suzhou 215123, People's Republic of China

[‡]Center for Joint Quantum Studies and Department of Physics, Tianjin University, Tianjin 300350, People's Republic of China

[#]Department of Applied Physics, The Hong Kong Polytechnic University, Hung Hom, Hong Kong SAR, People's Republic of China

[§]Department of Materials Science and Engineering, and ARC Centre of Excellence in Future Low-Energy Electronics Technologies (FLEET) Monash University, Clayton, Victoria 3800, Australia.

[//]These authors contributed equally to this work.

*Address correspondence to sjli@suda.edu.cn

Yuan, J., Sun, T., Hu, Z., Yu, W., Ma, W., Zhang, K., ... & Li, S. (2018). Wafer-scale fabrication of two-dimensional PtS2/PtSe2 heterojunctions for efficient and broad band photodetection. ACS applied materials & interfaces, 10(47), 40614-40622.

Abstract

A variety of fabrication methods for van der Waals heterostructures have been demonstrated; however, their wafer-scale deposition remains a challenge. Here we report a simple strategy to create few-layer $PtS_2/PtSe_2$ heterojunction photodiodes on a 2" SiO_2/Si substrate that is only limited by the size of work chamber of the equipment, offering throughputs necessary for practical applications. Theoretical simulation results show that the bandgap of PtS_2 is shrunk to half of its original size in the $PtS_2/PtSe_2$ heterostructure, while $PtSe_2$ is almost unchanged, indicating a limited response to the coupling. Both $PtSe_2$ and PtS_2 layers in the coupled system are still semiconductors. Dynamic photovoltaic switching in the heterojunctions is observed at zero-volt state under laser illuminations of 532 to 2200 nm wavelengths. The $PtS_2/PtSe_2$ photodiodes show excellent characteristics in terms of a high photoresponsivity of 361 mAW^{-1}, an external quantum efficiency (EQE) of 84%, and a fast response speed. The large-scale production of 2D photodidoes in this work accelerates the possibility of 2D materials for practical applications in the next-generation energy-efficient electronics.

Keywords: van der Waals heterostructures, wafer-scale fabrication, dynamic photovoltaic switching, photoresponsivity

Introduction

Heterojunctions, firstly invented in 1963 by Herbert Kroemer[1], have been essential building blocks for electronic and optoelectronic devices in the current semiconductor industry. Uses of such structures have been envisioned in nearly every type of micro devices, including biomedical devices, bipolar transistor, photodiodes, light-emitting diodes, and solar cells. As one of the most important existing optoelectronic devices, the photodiodes obviously play an important role in the applications of video imaging, optical communication, remote control and night vision[2, 3]. However, the diffused and drifted current across the junction can be remarkably influenced by the spatial extent of the depletion region generated in the conventional bulk semiconductor based junctions [4]. One possible way to break the limitation of the spatial extent and improve the performance of the devices is to create a heterojunction fabricated on ultra-thin materials[5, 6], that contains atomically sharp interfaces. Encouragingly, two-dimensional (2D) transition metal dichalcogenides (TMDs), one important member from the family of atomically thin van der Waals materials, has been widely studied and proved to be of great potential for the applications of future nano-electronics owing to their outstanding electronic, optical, mechanical properties and the strong light–matter interactions[7 8, 9]. Importantly, TMDs have extended bandgap tunability through composition,[10] thickness[11, 12] and possibly even strain control[13] offering infinite flexibility to design 2D junctions in more compelling ways[14, 15, 16, 17, 18, 19], which has shown great potential applications in photovoltaics, photodiodes and light emitters[11, 15, 20], and even could be possible to overcome some of the existing problems in conventional junction devices.[21]

Driven by the diversity and considerable wide coverage properties of TMDs materials, it is really feasible to fabricate artificial 2D van der Waals junctions,[18, 22] using either homogeneous or heterogeneous 2D materials. The formation of 2D homojunction can be formed by chemical/gate-induced electrical doping in the same nanoflake which lacks stability or makes device structures complicated.[23, 24, 25] The fabrication of 2D heterojunctions, however, mainly extends directly to materials

produced by exfoliation from the bulk counterpart using a variety of techniques[18, 26], but indirectly to those that can be deposited onto targeted substrates with facile control for the practical realization of high-volume manufacturing. Controlled and large-scale integration of more than one type of 2D material into a single structure still remains one of the most challenging tasks.

Recently, the group 10 metal based TMDs have attracted intense interests for the widely tunable band gap, large electrical conductivity and high air stability, which can well make up the drawbacks of graphene (zero band gap), most TMDs semiconductors (relatively large band gap), and black phosphorus (poor air stability). Representative examples of this family are platinum diselenide ($PtSe_2$) and platinum disulfide (PtS_2) that can be synthesized via a single step, *i.e.* direct selenization (or sulfuration) of the Pt substrate[27, 28]. Layered $PtSe_2$ has a tunable bandgap ranging from 1.2 eV (monolayer) to semimetal (bulk)[29], while layered PtS_2 has a bandgap varies from 1.6 eV in monolayer to 0.25 eV in bulk[30]. The large spread of bandgaps from visible to mid-infrared is similar to that of layered black phosphorus (BP), revealing potential for infrared electronic application. Compared to other extensively studied TMDs, such as MoS_2, WS_2, WSe_2 *etc*, field-effect transistors based on $PtSe_2$ layers exhibit higher mobility at room temperature, comparable to that of BP, suggesting that this material is applicable for high-performance electron transport devices[31]. Furthermore, few-layer $PtSe_2$ nanosheets have also been used to make infrared photodetectors with good photoresponsivity and fast response[31, 32]. Another case is few-layer PtS_2 phototransistor that shows high photoresponsivity and photoconductive gain due to the existence of trap states[33]. Although the optoelectronic properties of individual 2D group-10 TMDs have been preliminary studied, the comprehensive study of van der Waals like interlayer coupling of two different group-10 TMDs that can dramatically affect the band-structures and optoelectronic properties of 2D TMDs, and their 2D heterojunction diodes is still lacking. Moreover, existing TMDs/TMDs heterostructures reported to date display a spectral response that is mainly limited to visible wavelengths by the intrinsic band gap of the constituting materials[34]. By combining the advantages of ultrahigh stability and infrared photoresponse, 2D heterojunction diode based on group-

10 TMDs are promising for low-power and high frequency optoelectronics at infrared wavelengths.

Herein, we report a simple strategy to create few-layer van der Waals $PtS_2/PtSe_2$ heterojunctions on the surfaces of planar substrates to enable large-area manufacturing of 2D heterostructure diodes based on group-10 TMDs. Such a 2D heterojunction can simply be formed directly through selenization (or sulfuration) of the Pt substrate by changing the Se source from S on the Pt layer using an ambient pressure conversion process. The coverage, size, and shape of $PtSe_2$ onto PtS_2 film can be controlled as desired, and their thicknesses were determined by the thicknesses of the pre-deposited Pt film. Methods based on above process are naturally compatible with modern planar technologies, and they offer throughputs necessary for practical applications. Theoretical simulation results show that the bandgap of PtS_2 is shrunk to half of its original size in the $PtS_2/PtSe_2$ heterostructure, while $PtSe_2$ is almost unchanged, indicating a limited response to the coupling. Both $PtSe_2$ and PtS_2 layers in the coupled system are still semiconductors. Dynamic photovoltaic switching in the heterojunctions is observed at zero-volt state under laser illuminations of 532 to 2200 nm wavelengths. Upon optical illumination, the self-driven $PtS_2/PtSe_2$ photodiodes show excellent characteristics in terms of a high photoresponsivity of 361 mAW^{-1} and an external quantum efficiency of 84% at 532 nm. These diodes show promise for broad-band photodetection and solar energy harvesting.

Results and Discussion

The vertical heterojunction arrays (see Figure 1a and 1b for a microscope image) were obtained on an oxide silicon wafer with 300 nm thick silicon dioxide. They consist of few-layer PtS_2 and $PtSe_2$ films that were synthesized via direct selenization or sulfuration of the Pt substrate by changing the Se source from S on the Pt layer using an ambient pressure conversion process (see Methods for more details). Our fabrication process enables manufacturability of wafer-scale production of 2D heterojunctions for optoelectronic applications, and the maximum sample size obtained in our experiment is up to 2" in diameter limited by the work chamber of the equipment. From the high-

resolution optical microscopy images (Figure 1c), we can observe that the PtS_2 and $PtSe_2$ sheets are well-defined with very uniform contrast, irrespective of a single PtS_2 or $PtSe_2$ sheet or their overlap region, which is attributed to the delicate control of growth process, proper thermal budget and homogeneous thickness of PtS_2 and $PtSe_2$ sheets. The size of PtS_2 sheets and $PtSe_2$ sheets were designed to be 100 × 120 μm^2 and 100 × 100 μm^2, respectively. The reason that the overlap part did not mix together to form a lateral hybrid film of PtS_2-$PtSe_2$ is due to the two-step growth process we have employed. Atomic force microscopy (AFM) was used to probe the detailed surface morphology and the thicknesses of PtS_2, $PtSe_2$ sheets, and their vertical heterojunctions (Figure 1c). The AFM height profile indicates that the thickness of PtS_2/$PtSe_2$ heterojunction is ~5.1 nm. We have also measured the pure PtS_2 and $PtSe_2$ regions, respectively. The thicknesses of PtS_2 and $PtSe_2$ are measured to be ~2.4 and~2.7 nm, corresponding to five layers of PtS_2 and five layers of $PtSe_2$, respectively.[27]

Raman spectroscopy was utilized to identify and characterize the obtained PtS_2/$PtSe_2$ heterojunction films. Figure 1d shows the polarization-dependent Raman spectra of PtS_2/$PtSe_2$ heterojunction excited by the 633 nm laser. Both the feature peaks of PtS_2 and $PtSe_2$ are observed in the spectra. The as-grown $PtSe_2$ films show two feature peaks at ~176 cm^{-1} and ~210 cm^{-1} which correspond to the E_g and A_{1g} Raman active modes of $PtSe_2$, respectively. The E_g mode is an in-plane vibrational mode of Se atoms moving away from each other within the layer, while the A_{1g} mode is an out-of-plane vibration of Se atoms in opposing directions. There is also a small peak located at ~230 cm^{-1} which can be attributed to a longitudinal oscillation (LO) mode, similar to those observed in HfS_2, ZrS_2 and CdI_2.[35, 36] For PtS_2, three main peaks at about 307, 335, and 340 cm^{-1} can be assigned to E_g^1, A^1_{1g}, and A^2_{1g} phonon modes, respectively. On the basis of previously theoretical prediction and experimental observations[37], we know that these two out-of-plane modes, A^1_{1g} and A^2_{1g} are observable in the polarization-dependent Raman spectra of PtS_2, while their intensities are polarization-dependent. This phenomenon can also be found in our experiment as shown in Figure 1d, the difference is that the intensity disparity between these two modes are not as obvious as the previously reported results because the samples in our experiments are

formed with fine grains, as verified by X-ray diffraction (XRD), transmission electron microscopy (TEM) and Scanning TEM (STEM), as elucidated in the following part. Furthermore, Raman mapping images (inset of Figure 1d) indicate that the overlap part of the $PtSe_2$ and PtS_2 sheet are well-separated, where the $PtSe_2$ sheet stacks on the top of the PtS_2 sheet. The crystal structures of PtS_2 and $PtSe_2$ films were further explored by XRD, as shown in Figure S1. The layered PtS_2 and $PtSe_2$ film can be viewed as cleaved from the (0001) surface of the bulk PtS_2 and $PtSe_2$, where one Pt atom layer is sandwiched between two S or Se layers (PtS_2: JCPDS PDF No. 01-070-1140, $PtSe_2$: JCPDS PDF No. 01-088-2280). The main XRD diffraction peaks of $PtSe_2$ films are observed at about 17.6°, 34.6°, and 54.6°, which can be indexed to the (001), (002) and (003) crystal planes of $PtSe_2$, respectively, suggesting that $PtSe_2$ film grows along c-direction with (001) as bottom plane, which agrees very well with the previous reports.[38, 39] Similar results were found for the PtS_2 film. It is noteworthy that the diffraction peaks of Pt (111) disappeared after selenization or sulfuration which indicates a complete conversion of Pt into $PtSe_2$ and PtS_2 crystals.

The X-ray photoelectron spectroscopy (XPS) was also used to determinate the elemental binding energies of PtS_2, $PtSe_2$ sheets, and their vertical heterojunctions, as shown in Figure 1e. XPS spectra of the Pt 4f, Se 3d and S 2P regions were acquired on the heterojunction sample. The measurement results for the binding energies demonstrate the formation of PtS_2 and $PtSe_2$. The peak positions at 54.39 and 55.19 eV corresponds to the binding energy of Se^{2-}. Besides, two other peaks located at 73.9 and 77.3 eV of Pt 4f spectrum can be assigned to the Pt $4f_{2/7}$ and Pt $4f_{2/5}$. Two peaks at 162.3 and 163.6 eV of S 2p spectrum displayed are ascribed to binding energy of Pt-S bonds between adjacent Pt atoms and S-S bonds, respectively, similar to the previous results.[38, 40] To check the purity of the materials, Figure 1f displays the corresponding Pt, S and Se mapping images obtained by energy dispersive X-ray spectroscopy, which confirms that all the elements are homogeneously distributed throughout the entire structure.

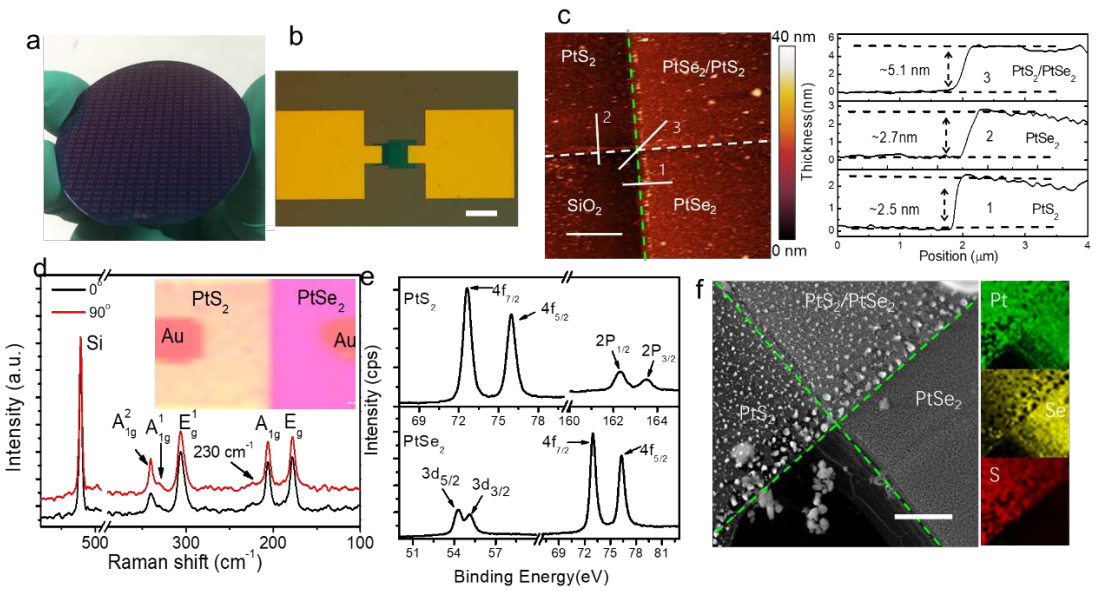

Figure 1

To further assess the microstructure, crystallinity, and elemental composition of the as-grown $PtS_2/PtSe_2$ vertical heterojunctions, the samples were transferred onto copper grid using the poly(methyl methacrylate) (PMMA) assisted transfer method[41] and investigated by TEM and STEM, as shown in Figure S2. The low-magnification TEM image (Figure S2b and Figure S2e) indicates that the $PtSe_2$ and PtS_2 nanosheets have good uniformity and continuity across the whole platelet. The inset in Fig. S2b shows the selected area electron diffraction (SAED) pattern of $PtSe_2$ nanosheet, which confirms the obtained sample is polycrystalline and the four distinguished red dashed circles are assigned to (001), (101), (111) and (201) planes with lattice spacings of 5.15, 2.77, 1.55 and 1.75 Å, respectively. The inset in Fig. S2e shows the SAED pattern of PtS_2 nanosheet, which confirms the obtained sample is polycrystalline and the four distinguished red dashed circles are assigned to (101), (102), (111) and (202) planes with lattice spacings of 2.61, 1.93, 1.65 and 1.29 Å, respectively. The high-resolution TEM (HRTEM) image of the $PtSe_2$ nanosheet in Figure S2c reveal clear lattice fringes with a lattice spacing of 0.287 nm corresponding to (101) facets of $PtSe_2$ nanosheet, while for the PtS_2 nanosheet, the lattice space is 0.261 nm as shown in Figure S2f.

To gain basic understanding of the electronic properties and band structure information of the $PtS_2/PtSe_2$ heterojunction, theoretical simulations were conducted using the Vienna ab initio simulation package. Details of the simulation process is

shown in Methods. The atomic geometries for layered $PtSe_2$, PtS_2 and coupled structure are shown in Figure 2 (a-c). The 1T phase is selected since it is the most stable structure in the simulation. The thickness of 5L-$PtSe_2$ and 5L-PtS_2 are 27.6 Å and 24.4 Å, comparable to the experimental value of 2.7 nm for $PtSe_2$ and 2.4 nm for PtS_2 respectively. Distances between adjacent Pt atoms in $PtSe_2$ and PtS_2 are 3.74 Å and 3.58 Å, respectively. When modeling coupled structure of $PtSe_2$ and PtS_2, the lateral lattice parameter of PtS_2 is slightly expanded in order to fix in the unit cell. Both 5L $PtSe_2$ and PtS_2 in 1T phase are observed to be semiconductors in experiments [31, 33, 38, 40]. Figure 2 d-f show the simulated band structures. 5L-$PtSe_2$ has an indirect band gap of 0.21 eV. The conductance band minimum (CBM) is settled between Gamma and M point, while the valance band maximum (VBM) is slightly offset from Gamma point. 5L-PtS_2 is also a semiconductor with indirect band gap of 0.89 eV. For the band structure of coupled system shown in panel f, the calculated band structure is only 0.03 eV, which seems to indicate a much more metallic feature, corresponding to a wide spread wavelength range. The plotted bands are a mixture of states from both PtS_2 and $PtSe_2$, which cannot represent the electronic properties of PtS_2 or $PtSe_2$ layers separately. It also needs to mention that adjusting the lattice parameter of PtS_2 slightly decreases its bandgap by around 0.3 eV according to simulation. In order to give a better estimation of the bandgap for each type of material, the projected density of states (PDOS) for Pt and Se/S atoms are also shown adjacent to band structures. By comparing the PDOS before and after the coupling, it can be found that the bandgap of PtS_2 is shrunk to half of its original size. Part of the shrink is caused by changing the lattice parameter. The PDOS of $PtSe_2$ is almost unchanged, indicating a limited response to the coupling. Both $PtSe_2$ and PtS_2 layers in the coupled system are still semiconductors since clear bandgaps are present in the PDOS plot, therefore it is naturally interesting to investigate the photovoltaic behavior of the heterostructure.

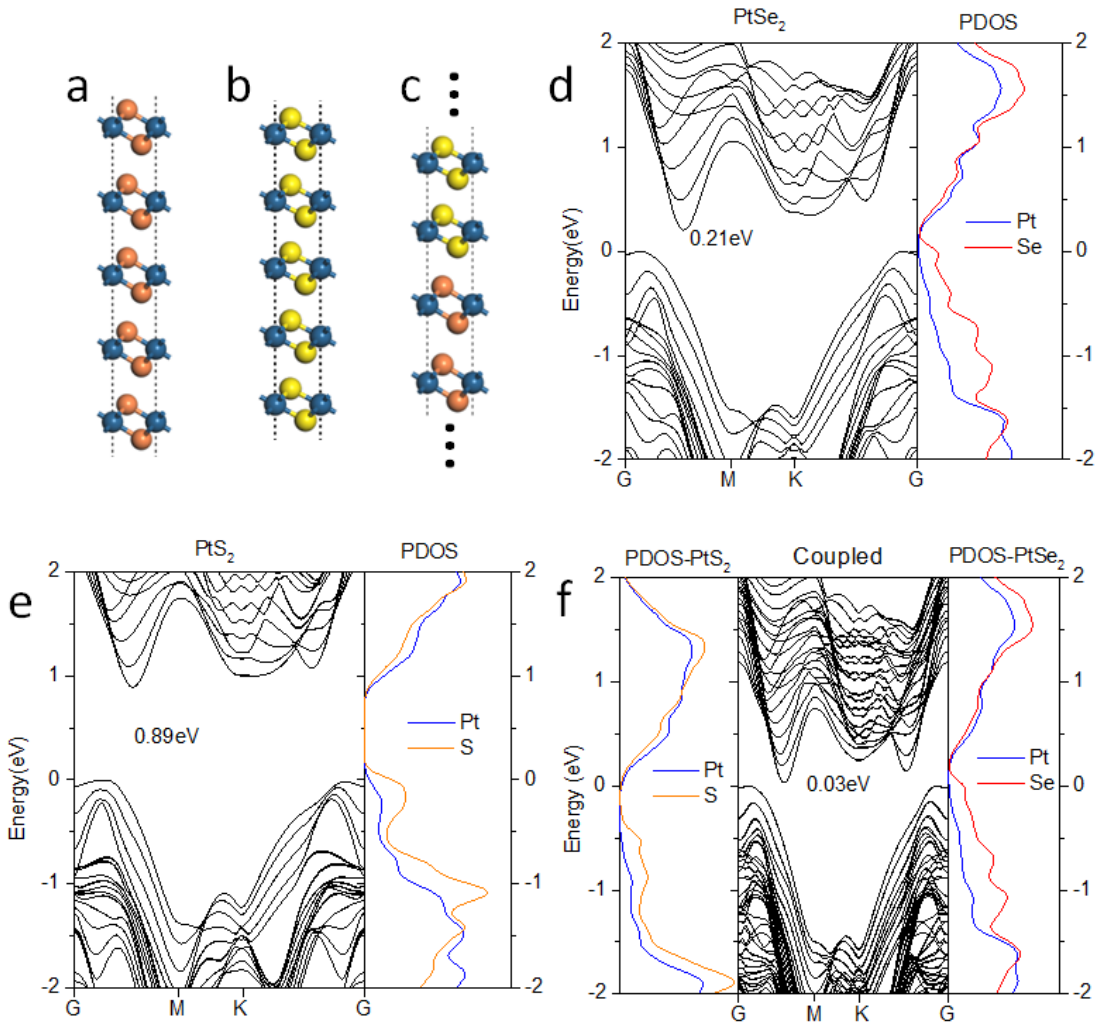

Figure 2. Atomic geometries. (a-c) and band structures. (d-f) of $PtSe_2$ and PtS_2. Blue, orange and yellow spheres in panel. (a-c) represent Pt, Se and S atoms respectively. 5L-$PtSe_2$ and 5L-PtS_2 are used in the coupled system in panel c. Some layers are not displayed in the figure in order to make the appearance clearer. The width of bandgap is inserted in band structure panels (d-f). Projected density of states (PDOS) for Pt and Se/S atoms are also shown adjacent to band structures.

Figure 3 shows a schematic illustration of the photodiode devices based on the PtS_2/$PtSe_2$ heterostructure, the corresponding current-voltage (*I*-*V*) characteristics in dark and under illumination, and the schematic band diagrams. The juction shows the typical diode *I*-*V* dependence as seen from Figure 3b. At positive bias voltage, the current gradually enhances with the applied voltage (V_{SD}) due to the increase of carrier density. The Figure S3 shows the perfect Ohmic contact on $PtSe_2$ and PtS_2, or a negligible barrier exists that does not significantly affect the rectifying characteristic.

The few-layered $PtS_2/PtSe_2$ heterojunction demonstrates low-voltage operation, the photovoltage (V_{ph}) and photocurrent (I_{ph}) are deduced to be 14.6 mV and 0.32 μA under a light power of 300 mW at 1064 nm, respectively.

To determine the band alignment at the $PtS_2/PtSe_2$ interface, we performed ultraviolet photoelectron spectroscopy (UPS) measurements to determine the band edge energies (Supporting Information, Figure S4). The results show that PtS_2 exhibits a little higher work function of 4.99 eV than that of $PtSe_2$ (4.93 eV). The work function offset (75 meV) between PtS_2 and $PtSe_2$ should block electron flow from the PtS_2 film to the $PtSe_2$ film after contact. Furthermore, the distance between the Fermi level (E_F) and valence band edge (Ev) in PtS_2 is larger than that in $PtSe_2$. To further evaluate the energy offset at the $PtS_2/PtSe_2$ heterojunction interface and identify direction of the photocarriers transportation, kelvin probe force microscopy (KPFM) measurements were performed and the representative KPFM image is shown in Figure S5a of Supporting Information. Figure S5b shows the surface potential taken along the solid lines in Figure S5a. The surface potential of the PtS_2 film is lower than that of the $PtSe_2$ film with a work function difference of approximately 35 meV. The difference of work function with UPS measurements in these two materials is because of the different environment in measurement, *i.e.* in air for KPFM measurement and in vacuum for UPS measurement. Notably, after contact, the surface potential of $PtSe_2/PtS_2$ film is promoted in comparison to pristine $PtSe_2$ film, suggesting electrons are transferred from PtS_2 to $PtSe_2$ after contact, in good agreement with the UPS measurement result. Therefore, the photo-induced current generation process in our 2D heterojunction is explained in the schematic band diagrams of Figure 3c,d. The estimation of energy levels are based on our theoretical calculation results along with the KPFM, UPS experimental verification. An energy band diagram of individual PtS_2 and $PtSe_2$ systems before heterojunction formation is shown in Figure 3c. After contact, the fermi levels in these two materials are shifted and so as to satisfy the equilibrium condition due to the work function mismatch, as shown in Figure 3d. The electrons diffuse from $PtSe_2$ to PtS_2 and forms a built-in electric field, which leads to band bending between these two materials so as to facilitate effective transportation of photo-excited carriers.

Figure 3d also illustrates the generation and transfer of photo-excited electron-hole pairs under light illumination. Under photo illumination, electron-hole pairs will be generated and then separated by the built-in electric field, part of the photogenerated electrons diffuse from PtS_2 towards the junction and are swept into $PtSe_2$, while holes move towards the $PtSe_2$. These photocarriers eventually are collected by the electrodes to give rise to a net current. The built-in electric field at the junction interface ensures that the device can operate at zero external bias voltage.

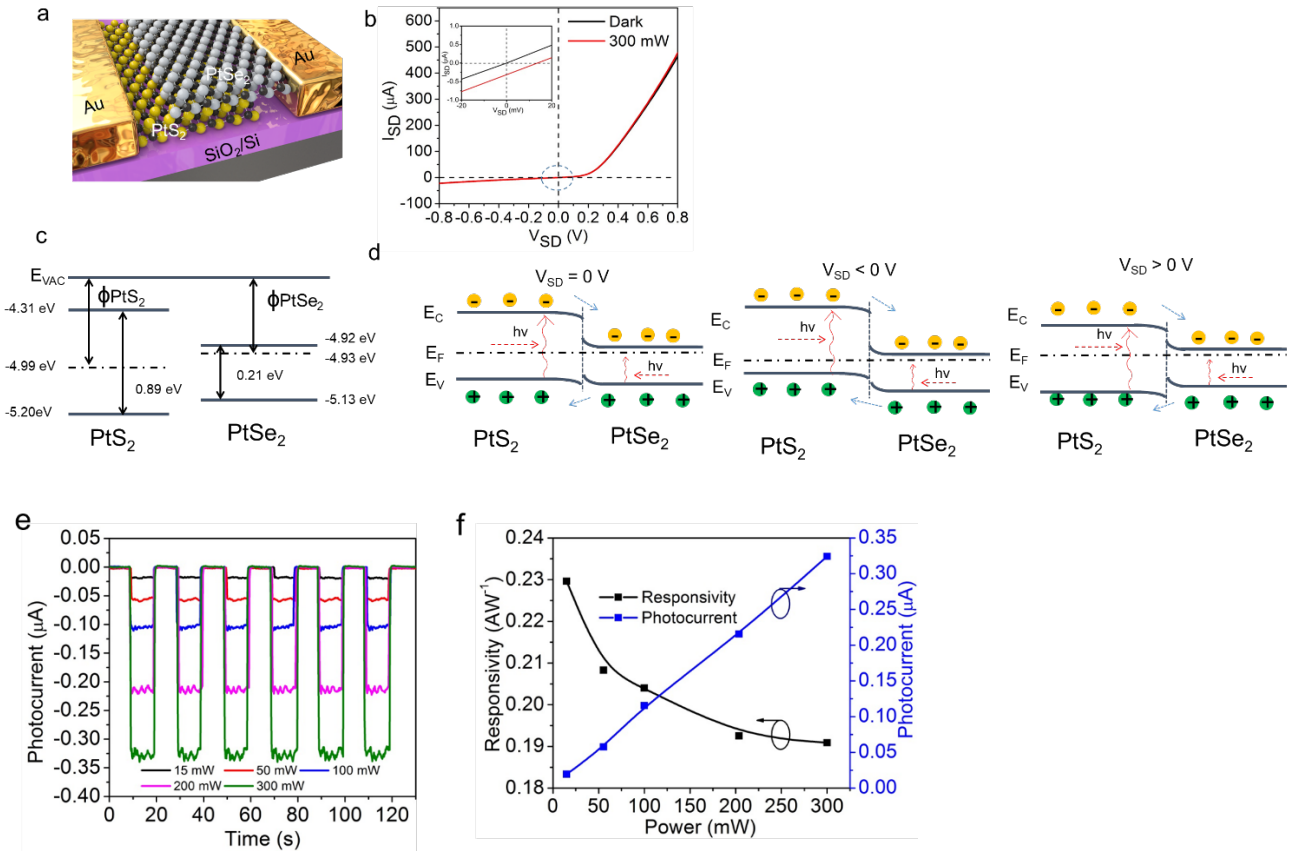

Figure 3

Figure 3e shows the typical photocurrent switching performance of the heterostructure at the infrared wavelength of 1064 nm without external bias voltages (V_{SD} = 0 V, V_G = 0 V). Dynamic photovoltaic switching is observed at zero-volt state under different laser powers. This kind of self-powered photodiode can have large numbers of applications like powerless communications, biological and chemical imaging in a wireless healthcare platform, and so on.

Responsivity is an important figure of merit for a photodetector and reflects its sensitivity to the incident light. Figure 3f shows the dependence of photocurrent and

responsivity on incident light power at zero-volt state. The photocurrent increases linearly while promoting the light power, while the responsivity decreases as the increase of incident power, in consistant with the behavious of other TMDs-based photodiode reported before.[42, 43] By contrast, a responsivity ($R = I_{photo}/P_{incident}$, I_{photo} is the photocurrent and $P_{incident}$ is the incident power) of 170 mAW^{-1} was obtained at low incident power (15 mW), which is comparable to must of reported values for heterojunction photodetectors at infrared wavelength. [43, 44]

With the aim to demonstrate the capability of the broadband ligh detection of our device, a series of photoelectric measurements were performed at different wavelengths. The temperal photoresponse with various wavelengths under the same light power (15 mW) is shown in Figure 4a. The device can be effectively switched ON and OFF while the light source is turned on and off even in the wavelength of 2200 nm (See the power-dependent photoresponse at 2200 nm in Figure S6, Supporting information). The overall profile of the wavelength-dependent photocurrent (Figure 4b) is highly consistent with the absorption spectrum of $PtSe_2$, due to the smaller bandgap and wider light absorption ability of $PtSe_2$. The wavelength-dependent responsivity (Figure 4c) under the same light power shows a highest value of about 308 mAW^{-1} under the visible light illumination (532 nm, 15 mW) and then decreases as the photon energy decreases. The power-dependent photoresponse was also investigated and the results are shown in Figure S7 of Supporting Information. An ultrahigh respnsivity of 361 mAW^{-1} is revealed, which is the best reported value among the reported values for TMDs-based photodiode.[45, 46] The external quantum efficiency EQE represent the ratio of the number of collected charge carriers to the number of incident photons. It can be calculated by the formula $EQE = (I_{photo}/P_{incident}) \times \frac{q\lambda}{hc}$, where λ is 532 nm of the wavelength and obtain EQE ~84%.[45, 47]

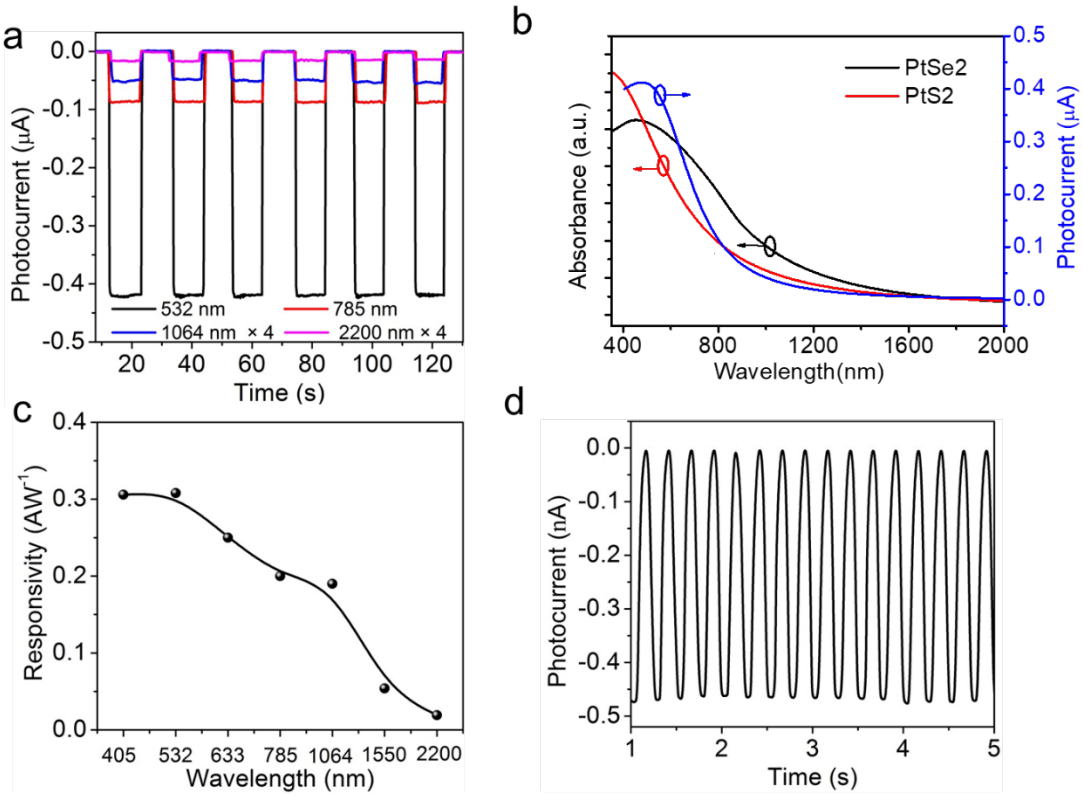

Figure 4

Table 1 PtS2/PtSe2 – Comparison with Other Heterojunction

Materials	Measurement Conditions	Responsivity (mA/W)	EQE	Response time (ms)	Range of response wavelength (nm)	Reference
$MoTe_2/MoS_2$	Vsd = 0 V 405 nm 800 nm	320 38	88% 6%	25 ms	400-800	*Adv. Mater. 2016, 28, 3216*
MoS_2/WSe_2	Vsd = -1 V 590 nm	11	1.5%	*	*	*Nano Lett. 2014, 14, 4785−4791*
MoS_2/WSe_2	Vsd = 0 V 532 nm	120	34%	*	500-800	*Nat. Nanotechnol. 2014, 9, 676*
BP/MoS_2	Vsd = -2 V 633 nm	518	0.3%	*	*	*ACS nano 2014 , 8 (8) :8292*
$PtS_2/PtSe_2$	Vsd = 0 V 532 nm 1064 nm	361 170	84% 20%	48 ms	405-2200	***This work***

We further investigate the response speed of $PtS_2/PtSe_2$ heterojunction photodetector by shining the device with pulsed light that is modulated by an optical chopper as shown in Figure 4d. The response of the photodiodes is very fast with the rise and decay times of 78 ms and 48 ms (Supporting Information, Figure S8a). The light response of the $PtS_2/PtSe_2$ heterojunction remains highly stable after 60 days under

the same illumination conditions, showing the excellent stability of the device in air at room temperatrue (Supporting Information, Figure S8b), which is very important for the practical implementation of this device in long-term operation. The performance of our $PtS_2/PtSe_2$ heterojunction devices is compared to other TMDs-based heterojunction photodiodes, as summarized in Table 1. The overall performance of our device is superior to existing MX_2/MX_2 (M = Mo, W; X = S, Se, Te) heterostructures in terms of working spectral range, responsivity, and EQE. We attribute the excellent photoresponse of $PtS_2/PtSe_2$ heterostructure to the effective carrier transportation and enhanced light absorption considering the semiconductor-to-semimetal bandgap transition in the coupled system. Note that the response time is comparable to pristine PtS_2 photodetector mainly limited by the existence of trap states[33], which may be further improved by optimizing the material quality and growth process.

CONCLUSION

In summary, $PtS_2/PtSe_2$ heterojunctions were produced by a two-step chemical vapor deposition methods, where the size, density, and geometry of 2D sheets can be adjusted as desired. Due to the built-in electric field at the interface of the heterojunction, it can be used for a self-driven photodetector without applying a source−drain bias. The self-driven $PtS_2/PtSe_2$ photodetectors showed excellent characteristics in terms of wide photoresponse range from 405 to 2200 nm, high photoresponsivity of 361 mAW^{-1} and EQE of 84% . The approach demonstrated here is also transplantable for making a variety of TMDs heterojunctions and may open up more possibilities toward large-scale optoelectronic applications.

Methods

Synthesis of the PtS_2/ $PtSe_2$ heterojunctions. A two-step chemical vapor deposition approach was developed to produce wafer-scale PtS_2/ $PtSe_2$ heterojunctions by using a double heating area furnace. In step one, photoresist was first spin-coated on the SiO_2/Si substrate and exposed to form the array of periodic square holes. Subsequently, 0.8 nm Pt was deposited by electron beam evaporation to the corresponding square holes. Then

the SiO_2/Si substrate with Pt was placed into the quartz tube at the downstream and heated to 600 ^oC and sulfur powder was then put at the upstream with 130 ^oC. Ar (argon) was introduced as the carrier gas (flow rate: 60 sccm). The SiO_2/Si substrates with Pt was maintained at 600 ^oC for 2 hours to form PtS_2. In step two, photoresist was spin-coated on the SiO_2/Si substrate with PtS_2 array and exposed again to form the periodic rectangle hole array on part of the PtS_2 sheets. After that, 0.8 nm Pt was then deposited by electron beam evaporation to form the periodic rectangle Pt arrays. Following, similar to the process of producing PtS_2 mentioned above, the furnace temperature was kept at 450 ^oC for 2 hours to prepare $PtSe_2$.

Fabrication of the PtS_2/ $PtSe_2$ heterojunctions devices. The PtS_2/ $PtSe_2$ heterojunctions devices fabrication process involves UV lithography to define the source-drain electrodes pattern and 5 nm Ti/80 nm Au evaporation to deposit the source -drain electrodes.

Characterization of PtS_2/ $PtSe_2$ heterojunctions. The morphology and structure of the synthesized nanomaterials were characterized by optical microscopy (OM, Olympus DX51), scanning electron microscopy (SEM, (FEI Quanta 200 FEG, acceleration voltage: 5 30 kV)), atomic force microscopy (AFM, Digital Instrument Nanoscope IIIA), transmission electron microscopy (TEM, FEI Tecnai F30, acceleration voltage: 200 kV), and micro-Raman spectroscopy (Horiba, LabRAM HR-800). X-ray photoelectron spectroscopy (XPS) was performed on a KRATOS AXIS Ultra DLD (KRATOS Analytical C.O.). Photoelectric measurements was performed on a probe station (Cascade M150) equipped with a semiconductor property analyzer (Keithley 4200) in ambient conditions. More photoelectrical properties of the devices are described in the Supporting Information.

Simulations of the energy band of the PtS_2 and $PtSe_2$: Simulations were conducted using the Vienna ab initio simulation package[48]. The wave function was described by a plane-wave basis set with projected augmented wave method[49, 50]. The exchange-correlation functional was simulated with the optB86b exchange function[51] and van der Waals density functional method[52, 53], which was found to be accurate in reproducing layered structures[54, 55, 56, 57]. Energy cutoff for the plane wave basis was set to 400 eV

in structural relaxations and increased to 500 eV in static calculations. Layered $PtSe_2$ and PtS_2 were modeled by a 1×1 supercell. 5L slab model was used for each type of materials, with a vacuum space of at least 20 Å in z direction. The k-mesh was sampled by a 3×3×1 k-mesh, accuracy tested by a 5×5×1 one. All atoms were relaxed until the residual force for each atom was less than 0.01 $eV \cdot Å^{-1}$.

Reference：

1. Kroemer H. A proposed class of hetero-junction injection lasers. *Proceedings of the IEEE* 1963, **51**(12)**:** 1782-1783.

2. Gong X, Tong M, Xia Y, Cai W, Moon JS, Cao Y*, et al.* High-detectivity polymer photodetectors with spectral response from 300 nm to 1450 nm. *Science* 2009, **325**(5948)**:** 1665-1667.

3. Mueller T, Xia F, Avouris P. Graphene photodetectors for high-speed optical communications. *Nat Photonics* 2010, **4**(5)**:** 297-301.

4. Lee GH, Cui X, Kim P. Atomically thin p-n junctions with van der Waals heterointerfaces. *Nature nanotechnology* 2014, **9**(9)**:** 676-681.

5. Britnell L, Ribeiro RM, Eckmann A, Jalil R, Belle BD, Mishchenko A*, et al.* Strong light-matter interactions in heterostructures of atomically thin films. *Science* 2013, **340**(6138)**:** 1311-1314.

6. Geim AK, Grigorieva IV. Van der Waals heterostructures. *Nature* 2013, **499**(7459)**:** 419.

7. Ahmad N, Younus HA, Chughtai AH, Verpoort F. Metal-organic molecular cages: applications of biochemical implications. *Chemical Society Reviews* 2015, **44**(1)**:** 9.

8. Lin S, Liu S, Yang Z, Li Y, Ng TW, Xu Z*, et al.* Solution‐Processable Ultrathin Black Phosphorus as an Effective Electron Transport Layer in Organic Photovoltaics. *Adv Funct Mater* 2016, **26**(6)**:** 864-871.

9. Lin S, Chui Y, Li Y, Shu PL. Liquid-phase exfoliation of black phosphorus and its applications. *Flatchem* 2017, **2:** 15-37.

10. Chhowalla M, Shin HS, Eda G, Li LJ, Loh KP, Zhang H. The chemistry of two-dimensional layered transition metal dichalcogenide nanosheets. *Nature Chemistry* 2013, **5**(4)**:** 263-275.

11. Xu ZQ, Zhang Y, Wang Z, Shen Y, Huang W, Xia X*, et al.* Atomically thin lateral p?n junction photodetector with large effective detection area. *2d Materials* 2016, **3**(4).

12. Ghorbaniasl M, Kuc A, Miró P, Heine T. A Single-Material Logical Junction Based on 2D Crystal PdS2. *Advanced materials* 2016, **28**(5)**:** 853.

13. Li P, Li L, Zeng XC. Tuning the electronic properties of monolayer and bilayer PtSe 2 via strain engineering. *J Mater Chem C* 2016, **4**(15)**:** 3106-3112.

14. Deng Y, Luo Z, Conrad NJ, Liu H, Gong Y, Najmaei S*, et al.* Black phosphorus-monolayer MoS2 van der Waals heterojunction p-n diode. *Acs Nano* 2014, **8**(8)**:** 8292-8299.

15. Furchi MM, Pospischil A, Libisch F, Burgdörfer J, Mueller T. Photovoltaic Effect in an Electrically Tunable van der Waals Heterojunction. *Nano letters* 2014, **14**(8)**:** 4785.

16. Lee CH, Lee GH, Zande AMVD, Chen W, Li Y, Han M*, et al.* Atomically thin p–n junctions with van der Waals heterointerfaces. *Nature Nanotechnology* 2014, **9**(9)**:** 676.

17. Cheng R, Li D, Zhou H, Wang C, Yin A, Jiang S*, et al.* Electroluminescence and photocurrent generation from atomically sharp WSe2/MoS2 heterojunction p-n diodes. *Nano letters* 2014, **14**(10)**:** 5590-5597.

18. Pezeshki A, Shokouh SHH, Nazari T, Oh K, Im S. Electric and Photovoltaic Behavior of a Few‐Layer α‐MoTe2/MoS2 Dichalcogenide Heterojunction. *Advanced materials* 2016, **28**(16)**:** 3216.

19. Roy T, Tosun M, Hettick M, Ahn GH, Hu C, Javey A. 2D-2D tunneling field-effect transistors using WSe2/SnSe2 heterostructures. *Appl Phys Lett* 2016, **108**(8)**:** 437-435.

20. S J, N U, H B, AB K, AF M. Mono- and bilayer WS2 light-emitting transistors. *Nano letters* 2014, **14**(4)**:** 2019.

21. Amani M, Burke RA, Proie RM, Dubey M. Flexible integrated circuits and multifunctional electronics based on single atomic layers of MoS2 and graphene. *Nanotechnology* 2015, **26**(11)**:** 115202.

22. Liu N, Tian H, Schwartz G, Tok JB-H, Ren T-L, Bao Z. Large-area, transparent, and flexible infrared photodetector fabricated using PN junctions formed by N-doping chemical vapor deposition grown graphene. *Nano letters* 2014, **14**(7)**:** 3702-3708.

23. Zhang Y, Ye J, Yomogida Y, Takenobu T, Iwasa Y. Formation of a stable p–n junction in a liquid-gated MoS2 ambipolar transistor. *Nano letters* 2013, **13**(7)**:** 3023-3028.

24. Pospischil A, Furchi MM, Mueller T. Solar-energy conversion and light emission in an atomic monolayer pn diode. *Nature nanotechnology* 2014, **9**(4)**:** 257-261.

25. Jo S, Ubrig N, Berger H, Kuzmenko AB, Morpurgo AF. Mono-and bilayer WS2 light-emitting transistors. *Nano letters* 2014, **14**(4)**:** 2019-2025.

26. Geim AK, Grigorieva IV. Van der Waals heterostructures. *Nature* 2013, **499**(7459)**:** 419-425.

27. Wang Y, Li L, Yao W, Song S, Sun J, Pan J*, et al.* Monolayer PtSe2, a New Semiconducting Transition-Metal-Dichalcogenide, Epitaxially Grown by Direct Selenization of Pt. *Nano letters* 2015, **15**(6)**:** 4013-4018.

28. Wang Z, Li Q, Besenbacher F, Dong M. Facile Synthesis of Single Crystal PtSe2 Nanosheets for

Nanoscale Electronics. *Advanced materials* 2016, **28**(46)**:** 10224.

29. Y W, L L, W Y, S S, JT S, J P*, et al.* Monolayer $PtSe_2$, a New Semiconducting Transition-Metal-Dichalcogenide, Epitaxially Grown by Direct Selenization of Pt. *Nano letters* 2015, **15**(6)**:** 4013.

30. Zhao Y, Qiao J, Yu P, Hu Z, Lin Z, Lau SP*, et al.* Extraordinarily strong interlayer interaction in 2D layered PtS2. *Adv Mater* 2016, **28**(12)**:** 2399-2407.

31. Zhao Y, Qiao J, Yu Z, Yu P, Xu K, Lau SP*, et al.* High-Electron-Mobility and Air-Stable 2D Layered PtSe2 FETs. *Advanced materials* 2017.

32. Peng YU, Wang Q, Yu X, Liu Z. Mid-infrared 2D Photodetector based on bilayer PtSe2. Lasers and Electro-Optics; 2016; 2016. p. STu4R.5.

33. Li L, Wang W, Chai Y, Li H, Tian M, Zhai T. Few‐Layered PtS2 Phototransistor on h‐BN with High Gain. *Adv Funct Mater* 2017**:** 1701011.

34. Zhang K, Zhang T, Cheng G, Li T, Wang S, Wei W*, et al.* Interlayer Transition and Infrared Photodetection in Atomically Thin Type-II MoTe2/MoS2 van der Waals Heterostructures. *Acs Nano* 2016, **10**(3)**:** 3852.

35. Cingolani A, Ferrara M, Lugarà M, Lévy F. The Raman Spectra of CdI2. *Solid State Commun* 1984, **50**(10)**:** 911-913.

36. Roubi L, Carlone C. Resonance Raman spectrum of HfS 2 and ZrS 2. *Physical Review B* 1988, **37**(12)**:** 6808.

37. O'Brien M, McEvoy N, Motta C, Zheng J-Y, Berner NC, Kotakoski J*, et al.* Raman characterization of platinum diselenide thin films. *2D Materials* 2016, **3**(2)**:** 021004.

38. Chia X, Adriano A, Lazar P, Sofer Z, Luxa J, Pumera M. Layered Platinum Dichalcogenides (PtS2, PtSe2, and PtTe2) Electrocatalysis: Monotonic Dependence on the Chalcogen Size. *Adv Funct Mater* 2016, **26**(24)**:** 4306-4318.

39. Zhang K, Yan M, Zhang H, Huang H, Arita M, Sun Z*, et al.* Experimental evidence of type-II Dirac fermions in PtSe2. *arXiv preprint arXiv:170304242* 2017.

40. Lin S, Liu Y, Hu Z, Lu W, Mak CH, Zeng L*, et al.* Tunable active edge sites in PtSe2 films towards hydrogen evolution reaction. *Nano Energy* 2017, **42:** 26-33.

41. Xu Z-Q, Zhang Y, Lin S, Zheng C, Zhong YL, Xia X*, et al.* Synthesis and transfer of large-area monolayer WS2 crystals: moving toward the recyclable use of sapphire substrates. *ACS nano* 2015, **9**(6)**:** 6178-6187.

42. Xue Y, Zhang Y, Liu Y, Liu H, Song J, Sophia J*, et al.* Scalable Production of a Few-Layer MoS2/WS2 Vertical Heterojunction Array and Its Application for Photodetectors. *ACS nano* 2016, **10**(1)**:** 573-580.

43. Wang L, Jie J, Shao Z, Zhang Q, Zhang X, Wang Y*, et al.* MoS2/Si Heterojunction with Vertically Standing Layered Structure for Ultrafast, High-Detectivity, Self-Driven Visible-Near Infrared Photodetectors. *Adv Funct Mater* 2015, **25**(19)**:** 2910-2919.

44. Zhang H, Zhang X, Liu C, Lee ST, Jie J. High-Responsivity, High-Detectivity, Ultrafast Topological Insulator Bi2Se3/Silicon Heterostructure Broadband Photodetectors. *ACS nano* 2016, **10**(5)**:** 5113-5122.

45. Pezeshki A, Shokouh SH, Nazari T, Oh K, Im S. Electric and Photovoltaic Behavior of a Few-Layer alpha-MoTe2 /MoS2 Dichalcogenide Heterojunction. *Adv Mater* 2016, **28**(16)**:** 3216-3222.

46. Lee CH, Lee GH, van der Zande AM, Chen W, Li Y, Han M*, et al.* Atomically thin p-n junctions with van der Waals heterointerfaces. *Nature nanotechnology* 2014, **9**(9)**:** 676-681.

47. Furchi MM, Pospischil A, Libisch F, Burgdorfer J, Mueller T. Photovoltaic effect in an electrically tunable van der Waals heterojunction. *Nano letters* 2014, **14**(8)**:** 4785-4791.

48. Kresse G, Furthmüller J. Efficient iterative schemes for ab initio total-energy calculations using a plane-wave basis set. *Physical Review B Condensed Matter* 1996, **54**(16)**:** 11169.

49. Blöchl PE. Projector Agmented-Wave Method. *Physical Review B* 1994, **50**(24)**:** 17953?17979.

50. Kresse G, Joubert D. From ultrasoft pseudopotentials to the projector augmented-wave method. *Physical Review B Condensed Matter* 1999, **59**(3)**:** 1758-1775.

51. Klimeš J, Bowler DR, Michaelides A. Van der Waals density functionals applied to solids. *Physical Review B* 2011, **83**(19)**:** 772-772.

52. Dion M, Rydberg H, Schröder E, Langreth DC, Lundqvist BI. van der Waals density functional for general geometries. *Physical review letters* 2004, **92**(24)**:** 246401.

53. Lee K, Murray éD, Kong L, Lundqvist BI, Langreth DC. A Higher-Accuracy van der Waals Density Functional. *Physical Review B* 2010, **82**(8)**:** 081101.

54. Hong J, Hu Z, Probert M, Li K, Lv D, Yang X*, et al.* Exploring atomic defects in molybdenum disulphide monolayers. *Nature communications* 2015, **6:** 6293.

55. Zhao Y, Qiao J, Yu Z, Yu P, Xu K, Lau SP*, et al.* High‐Electron‐Mobility and Air‐Stable 2D Layered PtSe2 FETs. *Adv Mater* 2017.

56. Qiao J, Kong X, Hu ZX, Yang F, Ji W. High-mobility transport anisotropy and linear dichroism in few-layer black phosphorus. *Nat Commun* 2014, **5:** 4475.

57. Wu JB, Hu ZX, Zhang X, Han WP, Lu Y, Shi W*, et al.* Interface Coupling in Twisted Multilayer Graphene by Resonant Raman Spectroscopy of Layer Breathing Modes. *ACS nano* 2015, **9**(7)**:** 7440.

Supporting information

Wafer-scale fabrication of 2D van der Waals heterojunctions for efficient and broadband photodetection

Jian Yuan[†,⁄⁄] *Tian sun,*[†,⁄⁄] *Zhixin Hu*[‡,⁄⁄] *Wenzhi Yu,*[†] *Weiliang Ma,*[†] *Kai Zhang, Qiaoliang Bao,*[§] *Shu Ping Lau,*[#] *Shenghuang Lin*[#] *and Shaojuan Li*[†,*]

[†]Institute of Functional Nano and Soft Materials (FUNSOM), Jiangsu Key Laboratory for Carbon-Based Functional Materials and Devices, Collaborative Innovation Center of Suzhou Nano Science and Technology, and Joint International Research Laboratory of Carbon-Based Functional Materials and Devices, Soochow University, Suzhou 215123, People's Republic of China

[‡]Center for Joint Quantum Studies and Department of Physics, Tianjin University, Tianjin 300350, People's Republic of China

[#]Department of Applied Physics, The Hong Kong Polytechnic University, Hung Hom, Hong Kong SAR, People's Republic of China

[§]Department of Materials Science and Engineering, and ARC Centre of Excellence in Future Low-Energy Electronics Technologies (FLEET) Monash University, Clayton, Victoria 3800, Australia.

[⁄⁄]These authors contributed equally to this work.

*Address correspondence to sjli@suda.edu.cn

Figure S1

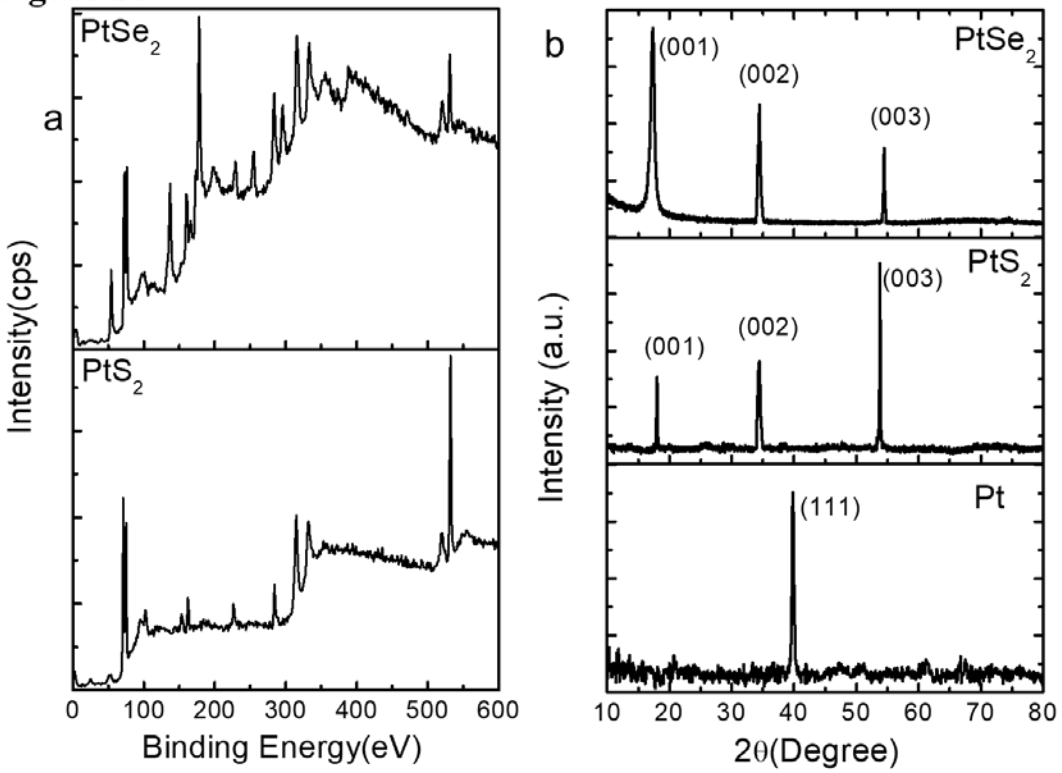

Figure S2

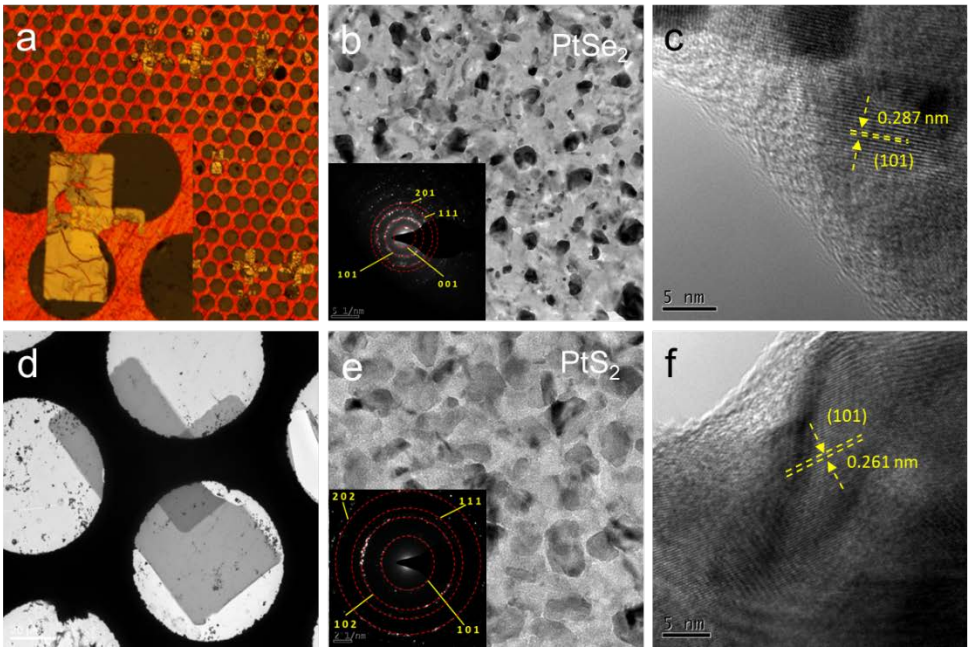

Figure S3

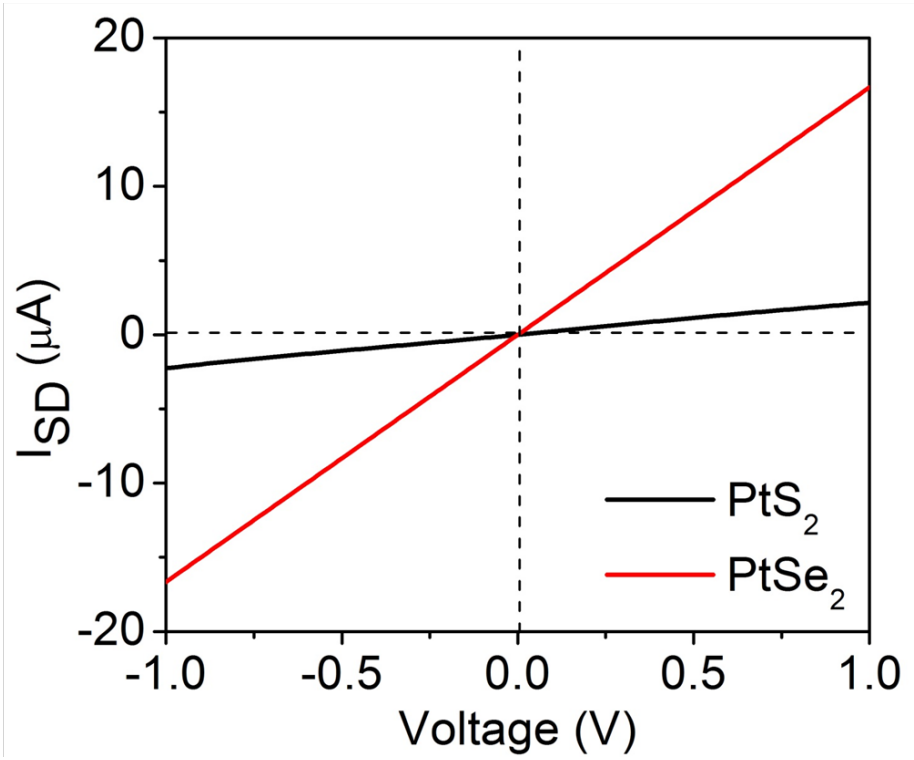

Figure S4

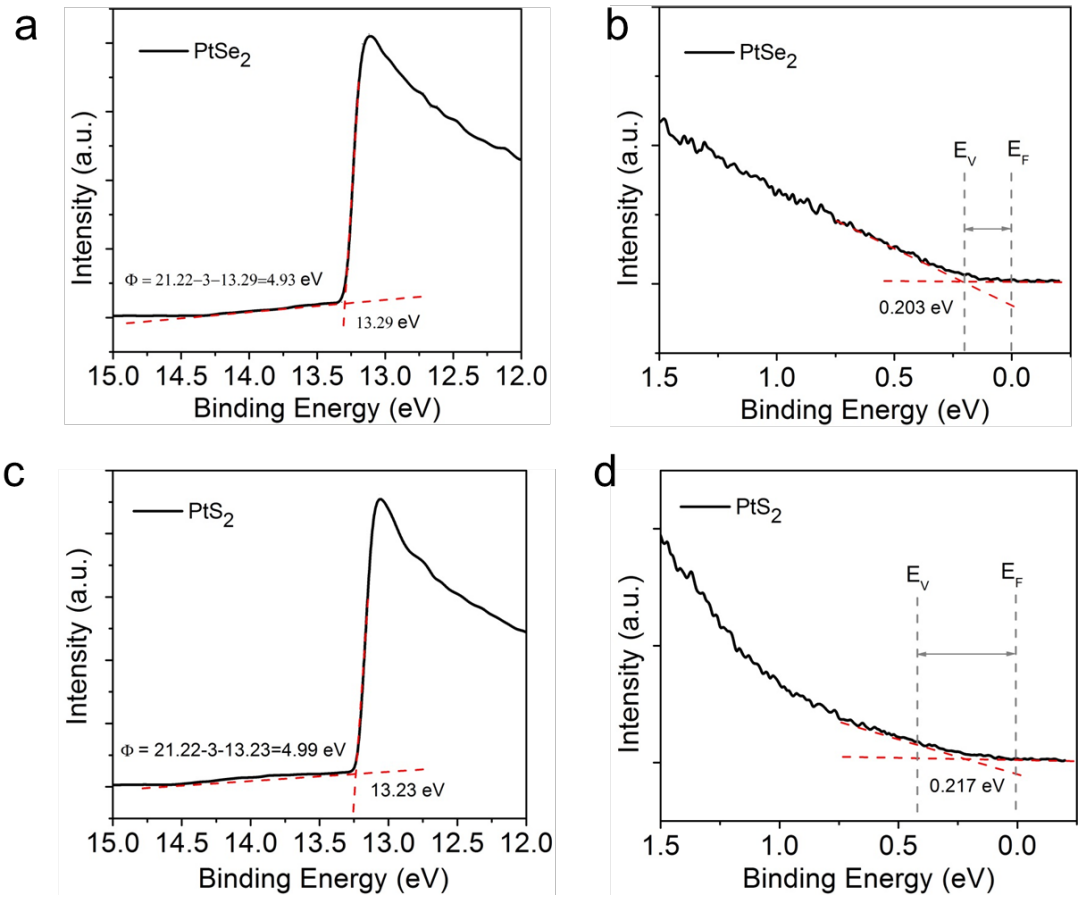

Figure S5

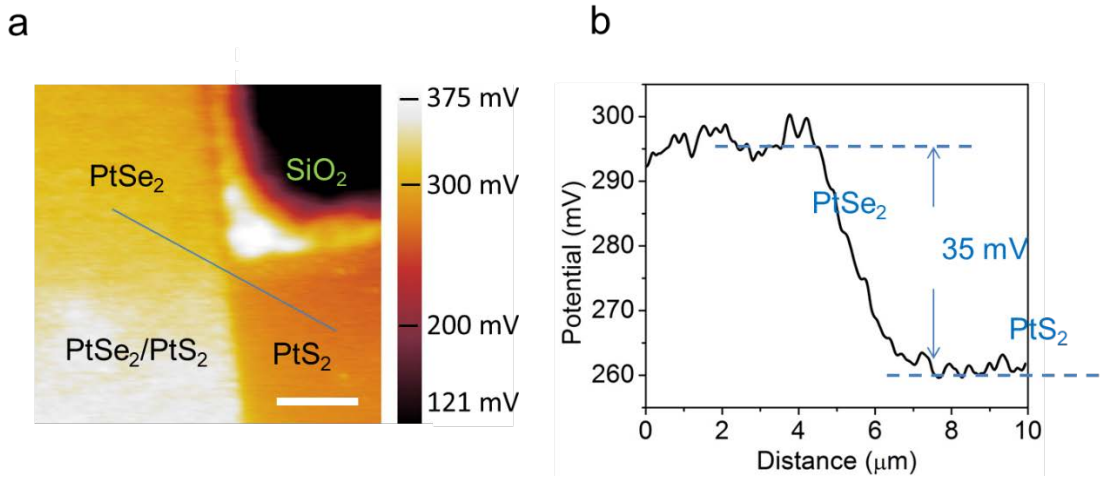

Figure S6

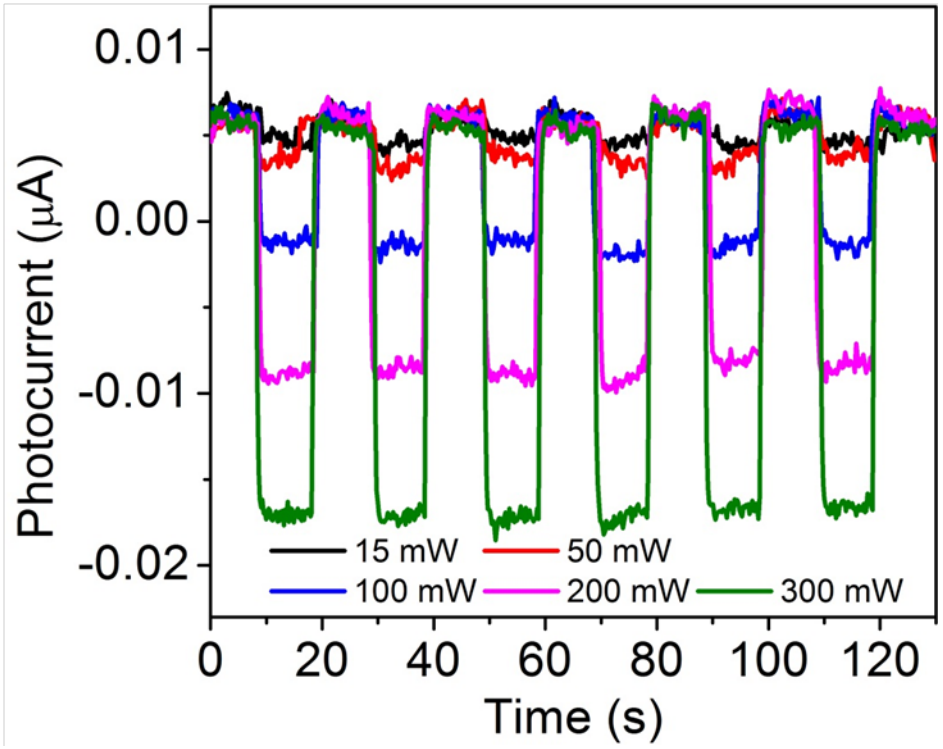

Figure S7

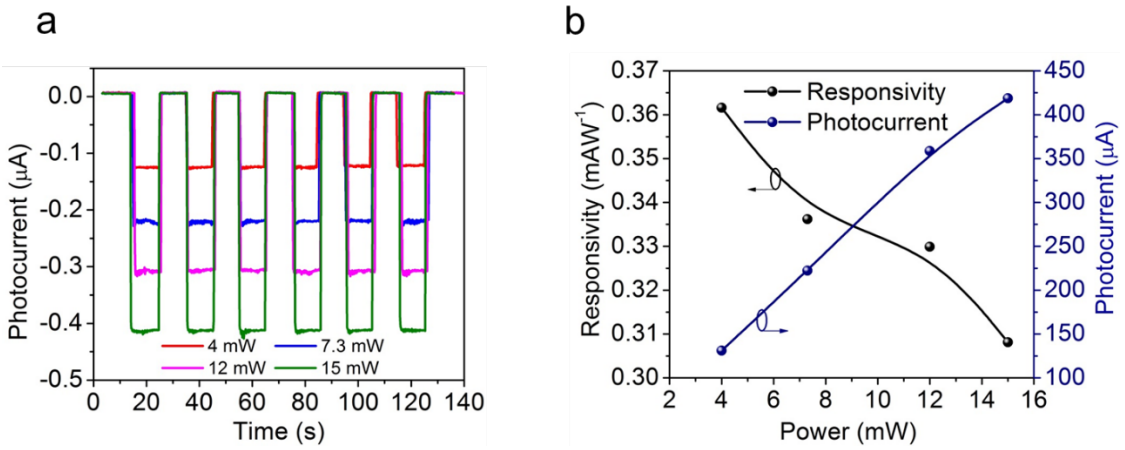

Figure S8

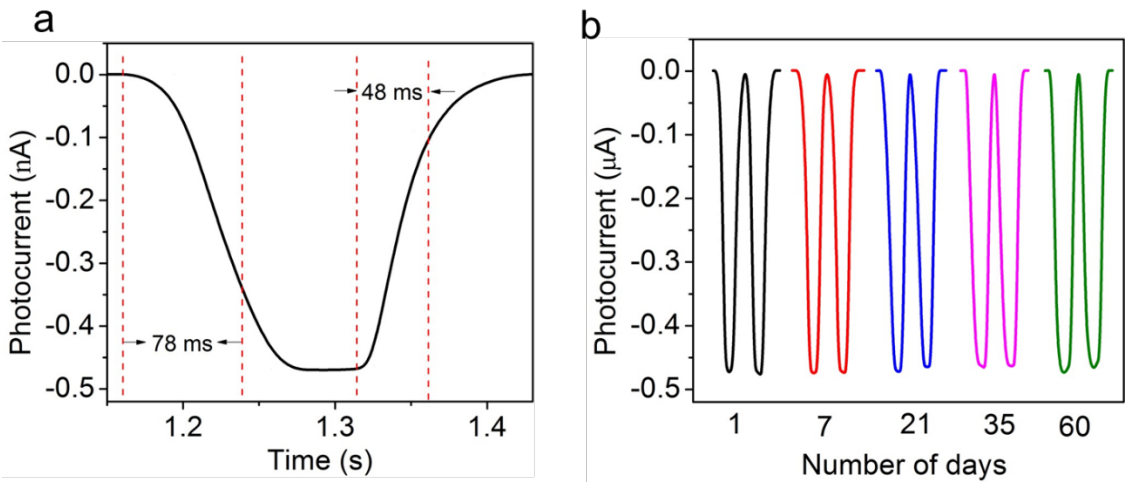
a
0.0
-0.1
-0.2
-0.3
-0.4
-0.5
Photocurrent (nA)
48 ms
78 ms
1.2
1.3
1.4
Time (s)
b
0.0
-0.1
-0.2
-0.3
-0.4
-0.5
Photocurrent (μA)
1
7
21
35
60
Number of days